Thermal Diffusivity of a Single Carbon Nanocoil: Uncovering the Correlation with Temperature and Domain Size

Chenghao Deng,[†,‡,#] Yanming Sun,[†,§,#] Lujun Pan,[†] Tianyu Wang,[‡] Yangsu Xie,[‡] Jing Liu,[‡] Bowen Zhu,[‡] and Xinwei Wang*[,‡]

[†]School of Physics and Optoelectronic Technology, Dalian University of Technology, No. 2 Linggong Road, Ganjingzi District, Dalian 116024, People's Republic of China

[‡]Department of Mechanical Engineering, Iowa State University, 2010 Black Engineering Building, Ames, Iowa 50011, United States

[§]College of Electronic Science and Technology, Shenzhen University, No. 3688 Nanhai Avenue, Shenzhen 518060, People's Republic of China

ABSTRACT: The helical geometries and polycrystalline–amorphous structure of carbon nanocoils (CNCs), an exotic class of low-dimensional carbon nanostructures, distinguish them from carbon nanotubes and graphene. These distinct structures result in very different energy transport from that in carbon nanotubes and graphene, leading to important roles in applications as wave absorbers, near-infrared sensors, and nanoelectromechanical sensors. Here we report a systematic study of the thermal diffusivity (α) and conductivity (κ) of CNCs from 290 to 10 K and uncover their property–structure aspects. Our room-temperature α study reveals a correlation between α and the line diameter (d): $\alpha = (5.43 \times 10^4 \times e^{-d/37.7} + 9.5) \times 10^{-7}$ m^2/s. Combined with the Raman-based grain size (L_a) characterization, α and L_a are correlated as $\alpha = [81.2 \times (L_a - 3.32)^{1.5} + 9.5] \times 10^{-7}$ m^2/s. With temperature decreasing from 290 K to 10 K, α has a 1–1.6-fold increase, and κ shows a peak around 75 K. To best understand the defect level and polycrystalline–amorphous structure of CNCs, the thermal reffusivity ($\Theta = \alpha^{-1}$) of CNCs is studied and compared with that of graphite and graphene foam from 290 K down to 10 K. Very interestingly, CNC's Θ linearly decreases with decreased temperature, while Θ of graphite and graphene foam have an exponential decrease. The extrapolated 0 K-limit Θ is determined by low-momentum phonon scattering and gives a structure domain size of CNC samples (d = 455, 353, and 334 nm) of 1.28, 2.03 and 3.24 nm. These sizes are coherent with the X-ray diffraction results (3.5 nm) and the Raman spectroscopy study and confirm the correlation among d, L_a, and α.

KEYWORDS: carbon nanocoil, thermal diffusivity, thermal conductivity, specific heat, domain size
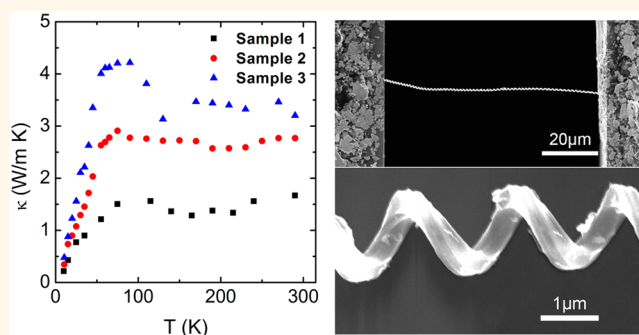
Carbon nanocoils (CNCs) are coiled carbon nanotubes (CNTs) with more or less incomplete crystalline structures.[1] Due to their particular helical structures, CNCs have significant potential to be used in field emitters,[2] wave absorbers,[3] near-infrared sensors,[4] nanoelectromechanical systems,[5,6] etc. Many studies have been carried out to investigate their electrical, mechanical, and thermal properties. The electrical conductivity of CNCs has been measured in the range of 20 to 200 S/cm, depending strongly on the crystallinity. The electron hopping contributes to the electrical conduction due to the disordered structures of CNCs.[7] The Young's modulus of CNCs ranging from several to several hundreds of GPa was reported. The annealing effect on the electrical and mechanical properties of CNCs has been reported owing to the improvement of crystallinity. Compared to the intensive research on the electrical and mechanical properties, the thermal properties of CNCs have not been well studied. Ma et al. measured the thermal conductivity of individual CNCs from the spectrum of thermal radiation induced by field emission, which was evaluated to be 38 W/m K by a one-dimensional thermal conduction model from the best fitted result.[8] Zhao et al. investigated the defect-dependent thermal conductivity of CNCs by nonequilibrium molecular dynamics simulations. The extreme reduction of thermal conductivity caused by defects and folds in CNCs was demonstrated.[9]
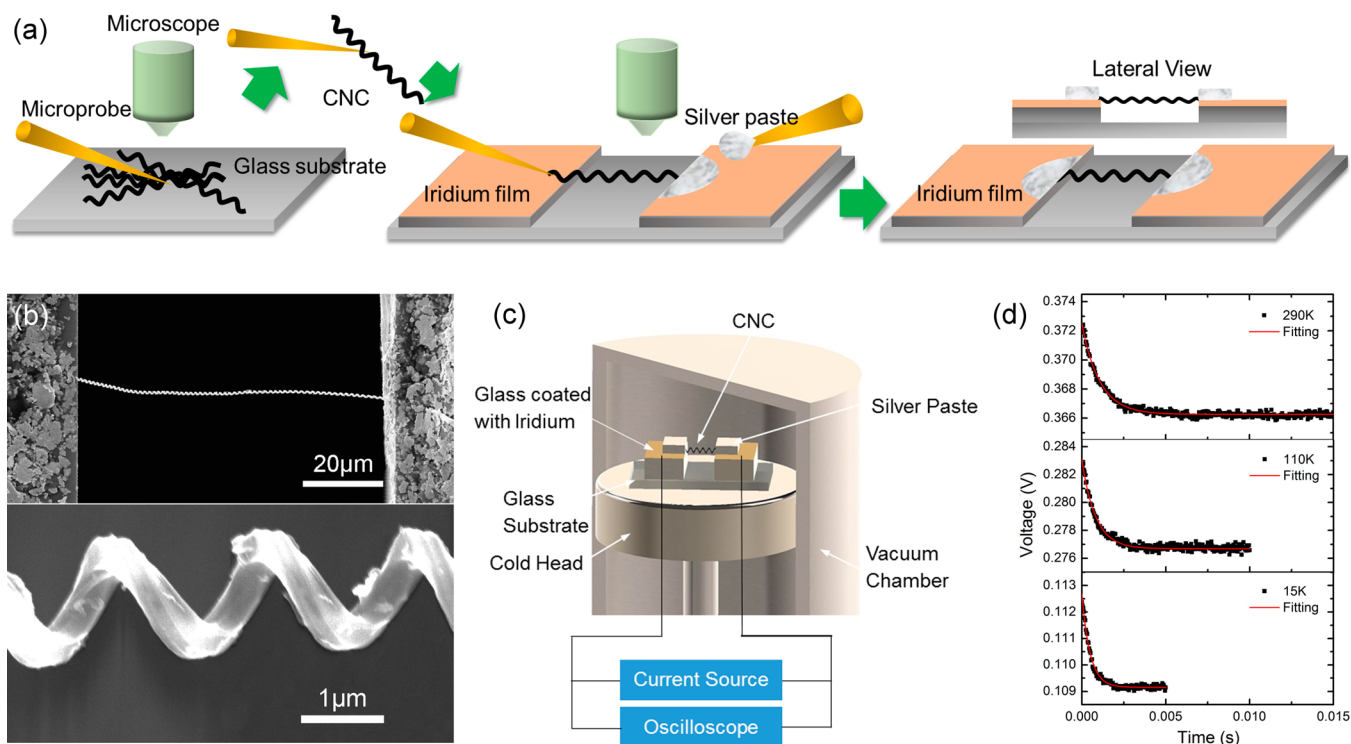
Figure 1. (a) Schematic of sample preparation. (b) SEM image of a typical sample and enlarged SEM image of a typical CNC. (c) Schematic of TET characterization. (d) Voltage−time evolution curve of a CNC sample (sample 3) at 290, 110, and 15 K recorded by oscilloscope.

In contrast to those of CNCs, the thermal properties of CNTs have been well investigated. There are four leading measurement techniques, which are the 3ω method, microfabricated suspended device method, optical heating and electrical thermal sensing method, and Raman thermal characterization. On the basis of these methods, the thermal conductivity of individual CNTs has been measured to be in the range of 300−6000 W/m K at room temperature (RT), depending strongly on the type and size of CNTs. Kim et al. fabricated a microsuspended CNT device. A heater resistor and a sensor resistor were employed to induce and measure the temperature drop across the CNT.[10] The thermal conductivity of an individual multiwalled CNT of diameter 14 nm was measured to be more than 3000 W/m K at RT. The mean free path (MFP) of phonons was estimated to be 500 nm at RT. From 8 to 370 K, a peak of the thermal conductivity was found at 320 K because the Umklapp phonon scattering became the dominant scattering source above 320 K. Pop et al. measured the thermal conductivity of individual single-walled CNTs with self-induced Joule heating from 300 to 800 K.[11] A peak thermal conductivity was also found around 320 K for a CNT of length 0.5 μm. When the length was increased, the peak shifted to a lower temperature due to the change of phonon-boundary scattering. Li et al. evaluated the thermal conductivity of individual CNTs by the Raman shift method, which almost eliminated the influence of the thermal contact resistance between the CNT and electrodes.[12]

The thermal properties of as-grown carbon nanofibers (CNFs), which have much poorer crystallinity than CNTs, have been studied as well. Yu et al. measured the thermal conductivity of an individual 152-nm-diameter CNF with a microfabricated suspended device.[13] A platinum heater and resistance thermometer were employed. From 150 to 310 K, the thermal conductivity increased from 7.5 to 13.5 W/m K.

Mayhew et al. measured the thermal conductivity of individual CNFs with a T-type probe experimental configuration in a scanning electron microscope (SEM) using the 3ω method.[14] The average thermal conductivity of the CNFs was 4.6 W/m K, which was increased to 163 W/m K after annealing at 2800 °C for 20 h. Heremans et al. reported the thermal conductivity of graphite fibers, which was around 38 W/m K at RT and improved by 50-fold after annealing at 3000 °C.[15]

Due to their helical morphology and internal structure different from CNTs and CNFs, CNCs exhibit different physical properties, which bring them advantages in some applications such as field emission, wave absorbing, or infrared sensing. To realize these applications, it is important to understand the thermal transport in CNCs, which has been seldom reported. Despite the intensive research, the difficulty in thermal characterization for nanostructured materials still exists, especially for giving overall thermal properties such as thermal diffusivity, thermal conductivity, and specific heat from RT down to quite low temperatures. This paper provides a feasible method of sample preparation and systematic thermal characterization for nanostructured materials. The thermal properties of carbon nanowires rely strongly on graphitization and crystallinity, especially for the almost disordered CNFs and CNCs. However, the relationship between thermal properties and structure of CNFs or CNCs at different temperatures has not been well studied, which is a research focus in this work. In this research, the transient electrothermal (TET) technique developed by our laboratory is applied to characterize the thermophysical properties of CNCs. The TET technique has been proven to be an accurate and reliable approach to measuring the thermal diffusivity of various solid materials, including conductive,[16] semiconductive, or nonconductive materials.[17,18] The obtained results have a high accuracy with less than 5% difference compared to the values in references.
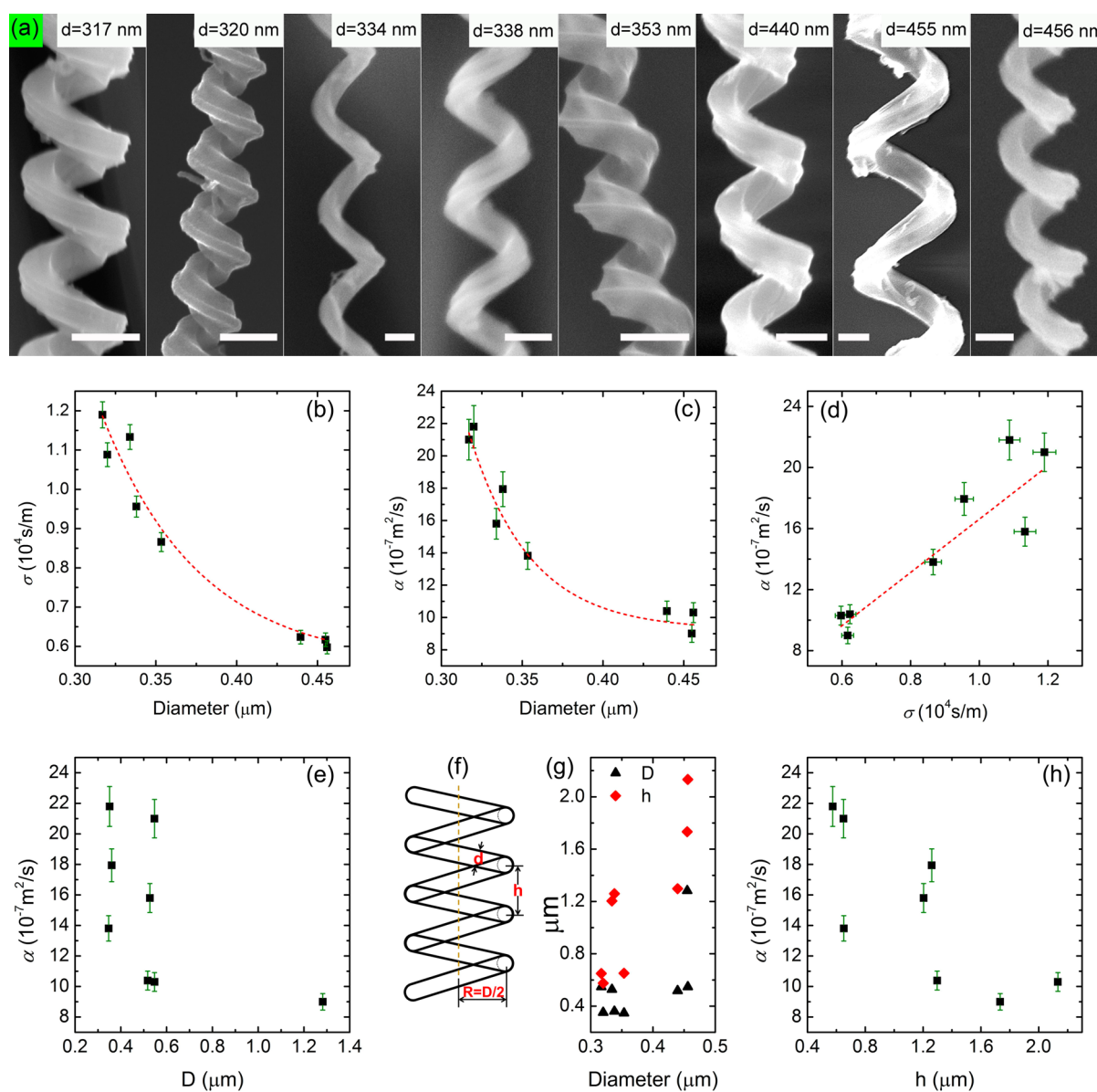
Figure 2. (a) SEM images of CNC samples with different line diameters. The scale bars are all 400 nm. (b) Electrical conductivity and (c) thermal diffusivity at RT of the CNCs in (a). (d) Correlation between the thermal diffusivity and electrical conductivity at RT. The relationship between the thermal diffusivity and (e) coil diameter and (h) pitch for the CNCs in (a). (f) Schematic representation of the helical morphology of CNCs. (g) Relationship between coil diameter, pitch, and line diameter of the CNCs in (a).

The detailed experimental process and principles for TET can be found in ref 16. Using the low-temperature TET technique, the temperature dependence of thermal conductivity, thermal diffusivity, specific heat, electrical conductivity, and domain size for CNCs are simultaneously obtained. The internal structure dependence of thermal properties and their relationship with electrical properties are analyzed.

RESULTS AND DISCUSSION

TET Characterization of Single CNCs. The CNCs were synthesized by a chemical vapor deposition (CVD) method. For thermal characterization, individual CNCs need to be suspended between two separated electrodes and connected electrically. The CNCs were first dispersed into ethanol, then dropped onto a glass substrate. Under an optical microscope, an individual CNC was extracted from a small CNC cluster on the glass substrate by using a tungsten microprobe with van der Waals (VDW) force (Figure 1a). Then the individual CNC was placed between two separated electrodes by micromanipulators when the CNC was attached onto the electrodes (iridium film) by VDW force. After that, another tungsten probe carrying a silver paste drop was employed to fix the CNC onto the electrodes. The upper and lower images in Figure 1b are the SEM image of a typical sample and the enlarged SEM image of a typical CNC, respectively.

The thermal diffusivity of CNC samples at different temperatures was measured using the TET technique. A schematic of the experimental setup is shown in Figure 1c. In a vacuum chamber, a step current was fed through the CNC samples by a current source. The amplitude of the step current was varied from 0.2 to 2 μA. The resistance of the CNCs will decrease under heating, resulting in a voltage decrease when the current is constant.[7] An oscilloscope was employed to record the voltage—time evolution curve. The TET characterization
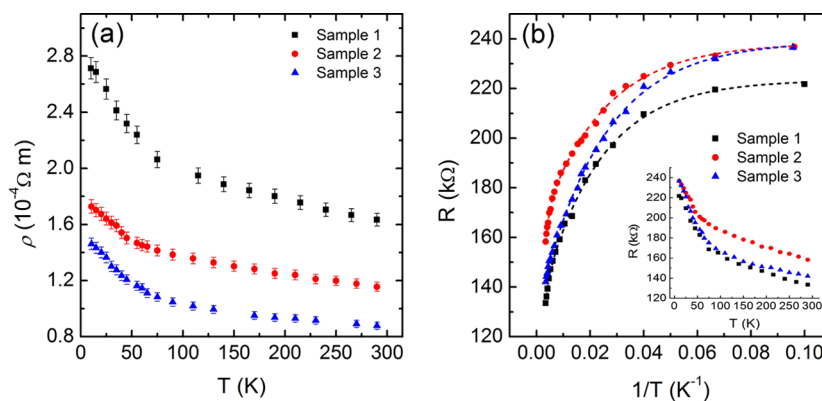
Figure 3. (a) Temperature-dependent electrical resistivity of three CNC samples. (b) Electrical resistance *versus* the reciprocal of temperature curves for the three CNC samples. The inset is the curves of electrical resistance *versus* temperature for the three samples.

was conducted from RT to 10 K. The pressure of the vacuum chamber was pumped to be lower than 0.5 mTorr during the whole measurement to reduce heat convection and water vapor condensation to a negligible level. The resistance or thermal diffusivity of the CNCs at RT almost stays the same before and after the long (>10 h) low-temperature tests under vacuum. It shows that the influence of adsorbed water is very little.

Due to joule heating induced by the step current, the average normalized temperature rise is given as[16]

$$T^* = \frac{48}{\pi^4} \sum_{m=1}^{\infty} \frac{1 - (-1)^m}{m^2} \frac{1 - \exp(-m^2\pi^2\alpha_{measure}t/L^2)}{m^2}$$

(1)

where $\alpha_{measure}$ is a combination of real thermal diffusivity and radiation effect. L and t are the total length of the CNC sample (considering its helical morphology) and evolution time, respectively. The temperature rise determines the voltage evolution. On the basis of the measured voltage evolution, the normalized temperature rise is expressed as $T^* = (V_{sample} - V_0)/(V_\infty - V_0)$, where V_0 and V_∞ are the initial voltage and steady voltage of the sample during TET heating, respectively. The theoretical fitting and iteration process for the voltage evolution curve were conducted with a MATLAB program to obtain the $\alpha_{measure}$, which gave the best fit of the experimental voltage curve. The $\alpha_{measure}$ combining real thermal diffusivity and the radiation effect is expressed as

$$\alpha_{measure} = \alpha + \frac{1}{\rho c_p} \frac{8\varepsilon_r\sigma\bar{T}^3}{d} \frac{L^2}{\pi^2}$$

(2)

where d, α, ρc_p, and ε_r are the line diameter, real thermal diffusivity, specific heat per unit volume, and effective heat emissivity of the CNC sample, respectively. $\sigma = 5.67 \times 10^{-8}$ W/m^2 K^4 is the Stefan–Boltzmann constant. The total length of the CNC is determined as $L = (l_0/h) \times \sqrt{[\pi(D - d)]^2 + h^2}$, where l_0, D, and h are the length, coil diameter, and pitch of the sample, respectively. In this research, the total length and line diameter of CNCs ranged from several tens to 200 μm and from 300 to 500 nm, respectively. On the basis of the experimental results, the effect of radiation on total thermal diffusivity is less than 5%. Therefore, the radiation effect is neglected and the $\alpha_{measure}$ is taken as the real thermal diffusivity.

TET characterizations were conducted from 290 to 10 K every 5–20 K. The datum collected became denser with a decrease in system temperature to observe a low-temperature

effect. The current amplitude was decreased gradually with a system temperature decrease to reduce the self-heating effect on the practical temperature of CNCs. The voltage evolutions of a typical CNC sample (sample 3) at 290, 110, and 15 K are presented in Figure 1d. With a temperature decrease, the time for relaxation to steady state is reduced, indicating an increased thermal diffusivity. The total length and line diameter of the sample are 142 μm and 334 nm, respectively. The thermal diffusivities are determined to be 1.58×10^{-6}, 2.70×10^{-6}, and 4.11×10^{-6} m^2/s at 290, 110, and 15 K, respectively, when the relative voltage reductions are 1.6%, 2.5%, and 2.7%, respectively. The signal-to-noise ratio is larger than 10. Using low-temperature TET, not only the thermal diffusivity but also electrical resistance, thermal conductivity, and volumetric specific heat at different temperatures can be obtained, which will be discussed later.

Electrical Conductivity and Thermal Diffusivity of CNCs at RT: Effect of Line Diameter. At RT, the electrical conductivity (σ) and thermal diffusivity (α) of eight CNC samples were measured with the TET technique, where σ was measured before TET heating. Their relationships with the line diameter of the CNCs are studied (Figure 2). Figure 2a shows the SEM images of the CNC samples, the line diameters (d) of which are marked in the images. The scale bars are all 400 nm. When d increases from 317 nm to 456 nm, σ decreases from 1.19×10^4 S/m to 0.60×10^4 S/m (Figure 2b). The results are very close to those in previous works including those measured by the four-probe method.[7,19,20] This confirms a good electrical contact between the CNC sample and the iridium electrode for our samples. On the other hand, good electrical contact represents good thermal contact. α decreases from 21.0×10^{-7} m^2/s to 10.3×10^{-7} m^2/s when d increases from 317 nm to 456 nm (Figure 2c). It shows a similar trend to that of the σ. The average value of the α and σ at RT are 15.0×10^{-7} m^2/s and 0.88×10^4 S/m, respectively. As reported by Sun *et al.*, CNCs with smaller line diameters have a larger graphite grain size and higher degree of graphitization, which lead to a higher σ.[7] This conclusion also applies to α. The differences in α and σ between the thin CNC (317 nm) and the thicker CNC (456 nm) reach 51% and 50%, respectively. Compared with CNT and CNF, CNC has particular helical geometries, as schematically shown in Figure 2f. The relationship between α and the coil diameter (D)/pitch (h) for the eight CNC samples is studied, which is presented in Figure 2e and h. α decreases against increased D or h. The coil diameter and pitch of CNCs are always correlated with the line diameter due to the catalyst-
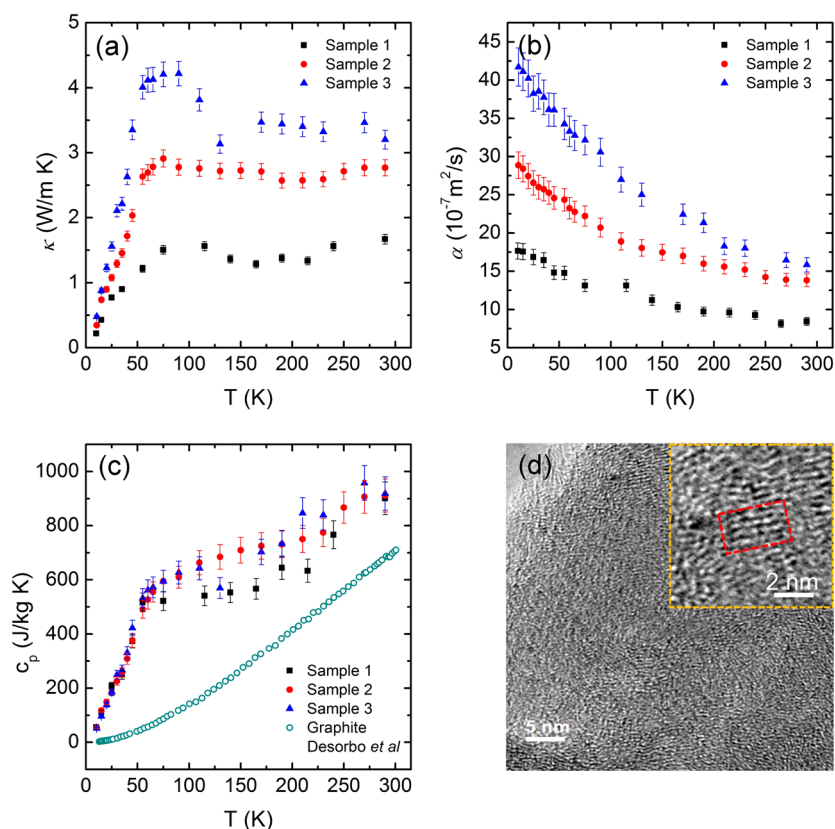
Figure 4. (a) Thermal conductivity, (b) thermal diffusivity, and (c) specific heat at different temperatures for the three CNC samples. (d) TEM image of a typical CNC. The inset is the enlarged TEM image of the CNC.

assisted CVD growth. The CNCs with a larger d often have a larger D and h, as presented in Figure 2g. The decrease in α at increased D/h originates from the negative correlation between α and d. The helical morphology itself has not shown an obvious effect on the thermal diffusivity of CNCs. The variation of α mainly comes from the difference in internal structure of the almost disordered CVD-synthesized CNCs. However, the helical geometries may exhibit a more significant influence on the thermal transport of more ordered helical multiwalled CNTs. As shown in Figure 2d, α exhibits a positive and linear correlation with σ. CNCs with better electrical conductivities have higher thermal conductivities (κ). Their relation shows some similarities to the Wiedemann–Franz law, although κ here is more sustained by phonons. But both conductivities reflect the effect of scattering by phonons and the structure of the material, so they are somehow correlated. In Figure 2b and c, we have fitted the correlation to uncover the line diameter effect and obtain the correlations as $\alpha = (5.43 \times 10^4 \times e^{-d/37.7} + 9.5) \times 10^{-7}$ m^2/s. The effect of the line diameter here indeed carries some intrinsic structure effect, specifically the effect of the grain size. In our Raman spectroscopy study, we have uncovered the correlation between the line diameter and CNC grain size. More discussions and in-depth analysis are given in a later section of the work.

Electron Transport: Effect of Temperature. We have prepared three samples to study their thermal and electrical properties down to 10 K. Figure 3a shows the electrical resistivity (ρ) versus temperature (T) curves of the three CNC samples. The inset of Figure 3b is the electrical resistance of the three CNC samples. The three CNC samples with different line diameters corresponding to 455, 353, and 334 nm are marked

as samples 1, 2, and 3, respectively. The total lengths of the three samples are 133, 134, and 142 μm, respectively. When the temperature decreases from 290 K to 10 K, the resistivity of the CNCs increases by 50–60%. As proposed by the previous work of Sun et al.,[7] the electron transport of CNCs is a combination of three mechanisms, which are the thermal activation model, nearest-neighbor hopping (NNH), and variable range hopping (VRH). At high temperatures (>100 K), the thermal activation dominates due to the semiconductor characteristic of CNCs. With a decrease in temperature, the thermal energy of electrons becomes too small compared with the thermal activation energy. As a consequence, the NNH conduction becomes the dominant electron transport process around 60 K. At lower temperatures, due to the further decrease of the thermal energy, electrons prefer to hop between non-nearest-neighboring localized states that have a lower energy difference, which is called VRH. The three samples share the similar trend of $\rho \sim T$ correlation. The differences between them come from different internal structure and graphitization.

Figure 3b shows the resistance (R) versus the reciprocal of temperature ($1/T$) curves of the three CNC samples, where $1/T$ represents the thermal energy of electrons. These curves can be exponentially fitted well and are used to obtain the value of dR/dT. The fitting curves are also shown in Figure 3b. The obtained dR/dT is employed to calculate the thermal conductivity of the sample and will be discussed later.

Thermal Transport and Properties: Correlation with Temperature. The thermal conductivity of CNCs was measured using the steady-state electrothermal (SET) technique from 290 to 10 K. When the temperature of the sample becomes stable, the temperature along the sample

derived from the governing equation for energy balance can be expressed as

$$T(x) = -\frac{I^2 R_\infty}{AL} \frac{(x^2 - Lx)}{2\kappa} + T_0 \tag{3}$$

where κ is the thermal conductivity. $T(x)$ is the temperature at position x. I is the applied current. R_∞ is the resistance of the sample at steady state. A and L are the cross-sectional area and total length of the CNC sample, respectively. T_0 is the temperature of the electrode corresponding to ambient temperature. The average temperature along the CNC sample is calculated as

$$\overline{T(x)} = \int_0^L T(x)\, dx/L = \frac{I^2 R_\infty L}{12\kappa A} + T_0 \tag{4}$$

Thus, the average temperature rise is $\Delta T = I^2 R_\infty L/12\kappa A$. The temperature rise ΔT can be calculated from resistance change, $\Delta R/(dR/dT)$, during our experiment, where ΔR is the resistance change before and after joule heating. As mentioned before, dR/dT can be calculated from the curve of resistance *versus* temperature (Figure 3b).

Combining the analysis above, the thermal conductivity κ is obtained as $\kappa = I^2 R_\infty L/(12A\Delta R/(dR/dT))$. Figure 4a and b are the thermal conductivity and thermal diffusivity of the three CNC samples, respectively. The thermal conductivities of the three samples at 290 K are 1.67 ± 0.08, 2.77 ± 0.12, and 3.20 ± 0.14 W/m K, respectively, which are comparable to the thermal conductivities of CNFs reported in refs 23 and 24. It is noted that our results are much lower than that of the CNC reported in ref 15 but are much larger than that of amorphous carbon.[21,22] With a temperature decrease, the thermal conductivity keeps increasing and reaches its maximum around 75 K for all three samples. The thermal conductivity of sample 3 shows a more obvious peak around 75 K than that of sample 1. The thermal conductivity of sample 1 above 75 K changes slightly with temperature. When the temperature continues to decrease after 75 K, the thermal conductivities go down rapidly, which reach 0.22 ± 0.01, 0.35 ± 0.02, and 0.48 ± 0.02 W/m K at 10 K, respectively, for the three samples. For the thermal conductivity peak around 75 K, many graphite-like materials in some works also show a similar peak near 75 K, including pyrolytic graphite deposited at 2250 °C in the work of Slack,[23] Canadian natural graphite in the work of Smith *et al.*,[24] and graphene with an adjustable defect level by the theoretical work of Nika *et al.*[25]

With the temperature decreasing, the thermal diffusivity continues to increase. This originates from the intensity reduction of lattice vibrations, which increases the MFP of phonons. From 290 to 10 K, the thermal diffusivities of samples 1, 2, and 3 increase by 109%, 109%, and 163%, respectively. For more disordered materials, such as glass, the thermal diffusivity exhibits a smaller change from RT to low temperature due to extremely small grain size. The MFP of phonons for glass in the work by Kittel was 0.8 nm at RT and increased by 88% when the temperature went down to 30 K.[26] It will be difficult to reveal more detailed features of the thermal transport in CNCs by Figure 4a and b, as they show similar trends of temperature correlation to graphite and graphene. In the next section, the thermal reffusivity study will clearly show the difference between CNCs and graphite and graphene.

The specific heat of CNCs is calculated as $c_p = \kappa/(\alpha\rho)$, where ρ is the mass density of CNCs, which is set as 2200 kg/m³,

corresponding to that of graphite.[23] On the basis of the obtained thermal diffusivity and thermal conductivity, the specific heat can be calculated and is shown in Figure 4c. First of all, for the three CNC samples, although they have different thermal conductivity, electrical resistivity, and thermal diffusivity, they share almost the same specific heat. This observation strongly proves the consistency and confidence of the measurement. At RT, the specific heats of the three CNC samples are 901, 911, and 919 J/kg K, which average 910 J/kg K. This value is between that of amorphous carbon (980 J/kg K)[27] and graphite (710 J/kg K).[28] With a decrease in temperature, the specific heat continues to decrease and approaches zero at the 0 K limit, which is physically reasonable. It is noted that the shape of the curves shows a big difference from that of highly oriented graphite, as depicted for comparison in Figure 4c. As reported by DeSorbo *et al.*, the specific heat of graphite can be fitted to T^2 from 10 to 300 K.[28] For the CNC samples in this research, the specific heats decrease slowly with decreased temperature above 75 K. Then the reduction rate increases rapidly after 75 K. One possible reason for the difference in the specific heat curve between CNCs and highly oriented graphite is the much lower Debye temperature of CNCs, which originates from the much lower degree of graphitization. The Debye temperature for graphite-like amorphous carbon was reported to be around 400 K,[21] while that of graphite is larger than 1800 K. CNCs are a kind of nanomaterial with sp² graphite grains embedded in an sp³ matrix. Their internal structures are between that of polycrystalline graphite and graphite-like amorphous carbon. The small sp² graphite grains in the highly disordered matrix can be observed from the transmission electron microscope (TEM) image of a typical CNC (Figure 4d). The inset in Figure 4d is an enlarged TEM image, where a small graphite grain is marked by a red square. The grain size is around 2.5 nm. The interlayer spacing for the grains is estimated to be 0.38 nm, which is close to that of graphite (0.335 nm). Thus, the Debye temperature of CNCs may be between that of graphite and graphite-like amorphous carbon. On the basis of this evaluation, the shape of the specific heat curve and the average specific heat at RT of CNCs are reasonable according to the Debye model. The polycrystalline−amorphous structure determines the low thermal conductivity of CNCs when boundary and defect scattering of phonons is quite strong. The thermal conductivity is a product of thermal diffusivity and specific heat. As the temperature decreases from 75 K to 10 K, the specific heat shows an approximately linear decreasing trend, which has also been found for some CNT materials. In this region, the rapid decrease of the specific heat dominates the change of thermal conductivity and determines the linear decrease of the thermal conductivity. Thermal transport is a complex process, especially for polycrystalline−amorphous structures. Future detailed theoretical analysis should consider the effect of amorphous structure, polycrystalline structure, the structure interface, grain boundaries, and the defects inside.

The errors involved in our measurement are summarized as 2% for line diameter, coil diameter, and pitch, 1% for length, 5% for MATLAB fitting, and 1% for electrical resistance. Using the error propagation theory, the error for electrical resistivity, thermal diffusivity, thermal conductivity, and specific heat are estimated as 2.8%, 6.0%, 4.5%, and 7.5%, respectively.

Thermal Reffusivity and Structure Domain Size. As shown in Figure 4, the thermal conductivity carries information about the phonon scattering and specific heat and is difficult to

use to obtain more information about the CNC structure. In this section, we study the reciprocal of thermal diffusivity (donated as Θ), which is called thermal reffusivity. It was first defined and used by Xu et al. to characterize the phonon thermal resistivity.[29] Just like electrical resistivity, thermal reffusivity is an intrinsic property of a material, which is solely determined by the phonon scattering inside materials. A classical model for phonon thermal conductivity can be expressed as $\kappa = \rho c_p \nu^2 \tau / 3$. Here ν is the phonon velocity, which changes little with temperature, but strongly depends on the phonon frequency and wave vector. τ is the relaxation time of the phonon, which is determined by Umklapp scattering (U-scattering), boundary, and defect scattering. However, the reciprocal of thermal conductivity (thermal resistivity) cannot fully describe the phonon scattering since ρc_p also changes with temperature. Therefore, the thermal reffusivity is defined as the reciprocal of thermal diffusivity to take out the specific heat effect.

The thermal reffusivity thus can be expressed as $\Theta = (3/\nu^2)(1/\tau)$. Note this formula is based on the single relaxation time approximation to reflect the most essential physics in thermal reffusivity. Full consideration of the phonon dispersion and the variation of phonon lifetime can be done and has been reported in work by Liu et al.[30] The relaxation time τ is inversely proportional to the phonon scattering intensity. Therefore, the thermal reffusivity directly reflects the phonon scattering. According to the Matthiessen rule, it is generally a good approximation to linearly add all the scattering effects for the overall scattering effect.

$$\frac{1}{\tau} = \frac{1}{\tau_U} + \frac{1}{\tau_{boundary}} + \frac{1}{\tau_{defects}} \quad (5)$$

where τ_U, $\tau_{boundary}$, and $\tau_{defects}$ are the relaxation time corresponding to U-scattering and boundary and defect scattering, respectively. τ_U increases exponentially with temperature, while $\tau_{defects}$ and $\tau_{boundary}$ are related to only the internal structure. Just like the electrical resistivity, the variation of thermal reffusivity versus temperature can be used to identify the residual value at the 0 K limit to evaluate the defect in the material. For materials with good crystallinity, the model of thermal reffusivity based on phonon scattering can be expressed as $\Theta = \Theta_0 + C \times \exp(-\theta_D/2T)$, where Θ_0 is the residual thermal reffusivity at 0 K limit. C is a fitting constant. θ_D is the Debye temperature. $\Theta_0 = (3/\nu^2)(1/\tau_{boundary} + 1/\tau_{defects})$. For a near-perfect material, Θ_0 is expected to be zero.

The thermal reffusivities of the three CNC samples are shown in Figure 5a. For comparison, the thermal reffusivities of graphite and graphene foam are shown in Figure 5b and c. The thermal reffusivity of graphite (b) and graphene foam (c) can be well explained by the model, where the data of which are obtained from the work of Ho et al.[31] and Xie et al.[32] The residual thermal reffusivity and Debye temperature for them are 43.3 s/m^2 and 1349 K and 1878 s/m^2 and 1813 K, respectively. However, the thermal reffusivity of the CNC samples does not follow the exponential model but obeys a linear relationship with temperature instead. We speculate this phenomenon comes from the polycrystalline−amorphous structure of CNCs. In addition to boundary and defect scattering, the transport of phonons has to overcome not only the scattering of lattice vibrations in sp^2 graphite grains but also the scattering of the sp^3 matrix. These two scattering sources all change with temperature, resulting in a combined scattering effect. For
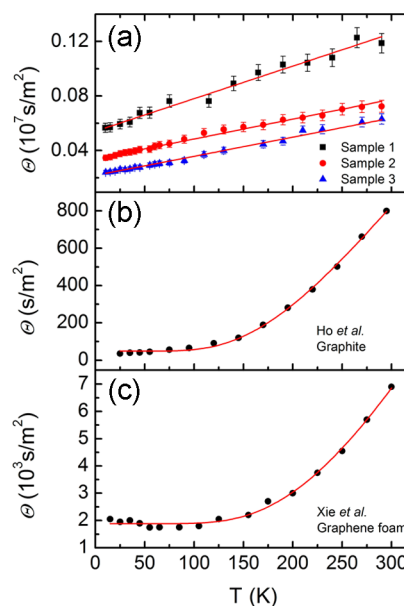
Figure 5. Thermal reffusivity of (a) CNC samples, (b) graphite, and (c) graphene foam at different temperatures.

highly oriented graphite, the contribution of the sp^3 structure can be neglected due to the high sp^2 to sp^3 ratio.

Despite the difference between experimental results and the thermal reffusivity model, the residual thermal reffusivity at the 0 K limit is still valid for CNCs, which is taken as the intersection of the fitting line with the vertical axis. The residual thermal reffusivities of the three CNC samples are 5.46 × 10^5, 3.44 × 10^5, and 2.15 × 10^5 s/m^2, respectively. With the knowledge of residual thermal reffusivity, the MFP of phonons (l_d) determined by boundary and defect scattering, which is termed domain size, can be calculated as $l_d = 3/(\Theta_0)$. Note this domain size is merely obtained from phonon scattering to reflect the size effect on phonon transport. It could not correspond to, but sometimes is quite close to, a real physical domain such as that uncovered by X-ray diffraction (XRD). For the calculation, the phonon velocity is estimated as 4300 m/s, which is taken from the work of Slack on pyrolytic graphite.[23] As a result, l_d for the three CNC samples are calculated as 1.28, 2.03, and 3.24 nm, respectively. This result indicates that CNCs with smaller line diameters have a larger domain size, which results in a higher thermal conductivity and electrical conductivity. For comparison, the line diameter d, domain size l_d, thermal conductivity κ, and electrical conductivity σ at 290 K of the three CNC samples are listed in Table 1.

Correlation between CNC Line Diameter and Internal Structure. To further understand the relationship between the internal structure and diameter of CNCs, Raman spectroscopy is employed. The CNCs were first dispersed into ethanol, then dropped onto 20 nm thick iridium film sputtered on a glass

Table 1. Line Diameter, Domain Size, Thermal Conductivity, and Electrical Conductivity at 290 K for the Three CNC Samples

sample	d (nm)	κ (W/m K)	σ (10^4 S/m)	l_d (nm)
1	455	1.67	0.61	1.28
2	353	2.77	0.87	2.03
3	334	3.20	1.14	3.24
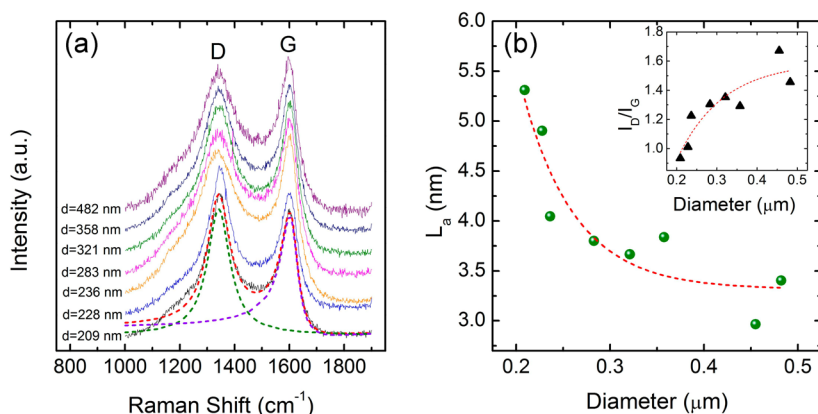
Figure 6. (a) Raman spectrum of eight individual CNCs with different line diameters. The D and G peaks are fitted by Lorentz and BWF functions, respectively, shown as the dashed lines for the CNC of 209 nm diameter. (b) Calculated grain size for the CNCs in (a). The inset is the area ratio of D to G peaks.

substrate. The iridium film was used to enhance the scattering signal of CNCs, while the Raman signal of suspended individual CNCs is too weak. Then eight individual CNCs with different line diameters were picked/identified under SEM for the next step, Raman characterization. Figure 6a shows the Raman spectrum of the eight CNC samples with different line diameters: 290 to 482 nm. The D peak around 1355 cm^{-1} and the G peak around 1581 cm^{-1} are two characteristic peaks for graphite-like materials, corresponding to the in-plane bond stretching motion of sp^2 atoms and the breathing mode of 6-fold aromatic rings occurring when disorders exist, respectively. Lorentz and BWF functions are employed to fit the D and G peaks, respectively,[33] shown as the dashed lines in Figure 6a. A smaller I_D/I_G, the area ratio of the D to G peaks, represents a larger sp^2 grain size and better crystallinity. I_D/I_G values for the eight CNC samples with different line diameters are shown in the inset of Figure 6b. I_D/I_G shows an increasing trend with increased line diameter. When the diameter increases from 200 nm to 455 nm, I_D/I_G increases from 0.93 to 1.67. This result demonstrates a significant structural variation with line diameter.

The ratio of the D to G peaks can be used to calculate the grain size, expressed as $I_D/I_G = C(\lambda)/L_a$, where $C(\lambda)$ and L_a are constants related to excitation wavelength and cluster diameter, respectively. $C(\lambda) = -12.6 + 0.033\lambda$, where λ is the wavelength of the excitation laser, which is 532 nm in this research.[33] Figure 6b shows the calculated L_a for the eight CNC samples. L_a decreases from 5.31 nm to 2.97 nm when the diameter increases from 200 nm to 455 nm. An exponential correlation is used to fit the results in the inset, and the grain size can be related to the line diameter (d) as $L_a = (76.4 \times e^{-d/56.6} + 3.32)$ nm. Combined with our study of the thermal diffusivity at RT for various line diameters, we can obtain a correlation between the thermal diffusivity and grain size: $\alpha = [81.2 \times (L_a - 3.32)^{1.5} + 9.5] \times 10^{-7}$ m^2/s. The thermal diffusivity and the grain size show a simple and positive power function relation. For the practical as-grown CNCs, the line diameter is in the range of 200 to 500 nm. The resulting L_a and α range between 5.55 and 3.33 nm and 2.79×10^{-5} and 9.60×10^{-7} m^2/s, respectively. It is seen that the change of thermal diffusivity is much larger than that of grain size. This difference indicates that the increase of thermal diffusivity comes not only from the increase of grain but also the improvement of grain arrangement.

Combining the thermal, electrical, and Raman characterization, it is reasonable to conclude that CVD-synthesized CNCs with smaller line diameters have better crystallinity, larger grain size, and higher electrical and thermal conductivity. It is noted that the grain size L_a calculated from Raman characterization is larger than the domain size l_d inferred from thermal characterization. The difference may come from the below four reasons. First, L_a is the in-plane correlation length that describes the sp^2 cluster size in the in-plane direction. It is derived from the scattering of the optical branch. l_d is the MFP of phonons induced by boundary and defect scattering, which is related to the scattering of the acoustic branch. These two phonon branches have different scattering behavior. Second, for carbon materials with sp^2 and sp^3 structures at the same time, the phonon velocity depends strongly on the internal structure and the ratio between sp^2 and sp^3 bonds.[22] The phonon velocity used in this research cannot precisely represent the real value of CNCs. Third, the static scattering originated from the sp^3 matrix is added to the scattering of the sp^2 grain boundary and reduces the value of the calculated MFP. For the more ordered structure, the effect of sp^3 matrix scattering will be less.

For further characterizing the internal structure of CNCs, XRD was carried out, and the result is shown in Figure 7. The
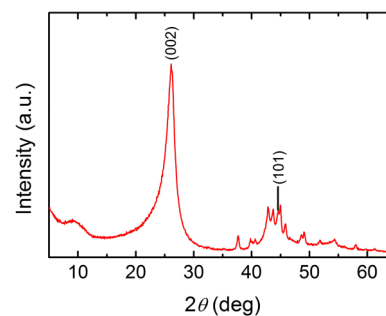
Figure 7. XRD characterization of CNCs.

main peak and another small peak marked in the graph correspond to the (002) and (101) crystal planes of graphite, respectively, while all the other peaks belong to cementite (Fe$_3$C). The peaks of Fe$_3$C come from the catalysts containing Fe. The size of the graphite grain is about 3.5 nm calculated from the main peak, which is very close to results of thermal and Raman characterization.

CNCs in this research are synthesized by CVD methods. The shape and size of catalyst particles have a significant influence on the formation of CNCs. Generally speaking, smaller catalyst particles have higher activity, which produce thinner and more ordered CNCs.[6,34] For more ordered CNCs, the scattering of graphite grain boundaries and defects will be weaker, resulting in a higher thermal diffusivity and thermal conductivity. It is a further topic in our lab on improving the thermal and electrical conductivities through annealing or controlling the synthesis process.

CONCLUSIONS

The thermophysical properties of CNCs were characterized with the TET technique from 290 K down to 10 K to investigate the correlation with line diameter, crystalline structure, and temperature. For eight CNC samples with different line diameters, the thermal diffusivity and electrical conductivity all showed negative correlation with the line diameter. The thermal diffusivity is correlated with the line diameter, and the thermal diffusivity and electrical conductivity are linearly correlated. As the temperature decreases from 290 to 10 K, the thermal diffusivity kept increasing, while the thermal conductivity showed a peak around 75 K. Compared to those at 290 K for the three CNC samples, the thermal conductivities decreased by 87%, 87%, and 85% at 10 K, while the thermal diffusivities increased by 109%, 109%, and 164%, respectively. The specific heat was found to be 910 J/kg K on average at RT, which is between that of graphite and amorphous carbon. With a decrease in temperature, the specific heat continues to decrease, and it showed a higher reduction rate after 75 K. Using the concept of thermal reffusivity, the defect level of CNCs was estimated. The thermal reffusivity of CNCs linearly decreased as the temperature decreased, while graphite and graphene have an exponential-like relation with temperature. The residual thermal reffusivity at the 0 K limit was used to calculate the domain size for the three CNC samples as 1.28, 2.03, and 3.24 nm. Our Raman spectroscopy study gave a correlation between line diameter and grain size as $L_a = (76.4 \times e^{-d/56.6} + 3.32)$ nm. At RT, the thermal diffusivity is correlated with the grain size as $\alpha = [81.2 \times (L_a - 3.32)^{1.5} + 9.5] \times 10^{-7}$ m^2/s. It is conclusive that CNCs with smaller line diameters exhibited better crystallinity and higher thermal conductivity and electrical conductivity. The activity difference between catalyst particles during the growth of CNCs was considered to be the main reason for the difference in crystallinity.

METHODS

CNC Synthesis. The CNCs were synthesized by a CVD method.[35] A 0.2 mol/L solution consisting of Fe$_2$ (SO$_4$)$_3$·9H$_2$O, SnCl$_2$·5H$_2$O, and deionized water served as the catalyst precursor. The catalyst was first dipped on the quartz substrate and then calcined at 710 °C for 30 min in an argon atmosphere with an Ar flow rate of 365 sccm. At last, the carbon deposits were achieved at 710 °C for 1 h by introducing acetylene and argon gases with flow rates of 15 and 325 sccm, respectively.

TET Characterization. The CNCs were suspended between two separated electrodes under an optical microscope suspended by silver paste with the help of micromanipulators and microprobes. The electrodes were prepared by sputtering 100 nm iridium film on glass substrates. Then the two separated electrodes were fixed onto a larger glass substrate with a 50−100 μm gap between them. The TET characterization was conducted from 290 to 10 K with atmospheric pressure lower than 0.5 mTorr. A Janis closed cycle refrigerator system

was utilized to provide a stable environmental temperature from 290 to 10 K. The sample was placed on the stage of a cold head. The whole stage was then shielded with a radiation shield and sealed with a clamped vacuum chamber. The amplitude and frequency of the step current fed through the CNCs ranged from 0.2 to 2 μA and from 10 to 20 Hz, respectively. The voltage change during TET heating recorded by an oscilloscope was less than 3% to reduce the self-heating effect on the practical temperature of the CNCs with a signal-to-noise ratio larger than 10.

Raman Characterization. The CNCs were first dispersed into ethanol, then dropped onto a 20 nm thick iridium film sputtered on a glass substrate, where the iridium film was used to enhance the scattering signal of CNCs. The individual CNCs with different line diameters were picked/identified under SEM for Raman study. The Raman spectrum of CNCs was obtained by a Raman spectroscopy instrument with a 100× objective lens, exciting laser with 532 nm wavelength, and power less than 1 mW, with a 30 s integration time.

AUTHOR INFORMATION

Corresponding Author

*Tel (X. Wang): +1 515 2948023. E-mail: xwang3@iastate.edu.

Author Contributions

#C. Deng and Y. Sun contributed equally to this work.

Notes

The authors declare no competing financial interest.

REFERENCES

(1) Pan, L. J.; Zhang, M.; Nakayama, Y. Growth Mechanism of Carbon Nanocoils. *J. Appl. Phys.* **2002**, *91*, 10058−10061.

(2) Hokushin, S.; Pan, L.; Konishi, Y.; Tanaka, H.; Nakayama, Y. Field Emission Properties and Structural Changes of A Stand-alone Carbon Nanocoil. *Jpn. J. Appl. Phys. 2* **2007**, *46*, L565−L567.

(3) Tang, N. J.; Yang, Y.; Lin, K. J.; Zhong, W.; Au, C. T.; Du, Y. W. Synthesis of Plait-Like Carbon Nanocoils in Ultrahigh Yield, and Their Microwave Absorption Properties. *J. Phys. Chem. C* **2008**, *112*, 10061−10067.

(4) Ma, H.; Pan, L.; Zhao, Q.; Peng, W. Near-infrared Response of A Single Carbon Nanocoil. *Nanoscale* **2013**, *5*, 1153−1158.

(5) Volodin, A.; Van Haesendonck, C.; Tarkiainen, R.; Ahlskog, M.; Fonseca, A.; Nagy, J. B. AFM Detection of The Mechanical Resonances of Coiled Carbon Nanotubes. *Appl. Phys. A: Mater. Sci. Process.* **2001**, *72*, S75−S78.

(6) Deng, C. H.; Pan, L. J.; Ma, H.; Cui, R. X. Electromechanical Vibration of Carbon Nanocoils. *Carbon* **2015**, *81*, 758−766.

(7) Sun, Y. M.; Wang, C. W.; Pan, L. J.; Fu, X.; Yin, P. H.; Zou, H. L. Electrical Conductivity of Single Polycrystalline-Amorphous Carbon Nanocoils. *Carbon* **2016**, *98*, 285−290.

(8) Ma, H.; Pan, L. J.; Zhao, Q.; Zhao, Z. B.; Qiu, J. S. Thermal Conductivity of A Single Carbon Nanocoil Measured by Field-emission Induced Thermal Radiation. *Carbon* **2012**, *50*, 778−783.

(9) Zhao, J. H.; Wu, J. Y.; Jiang, J. W.; Lu, L. X.; Zhang, Z. L.; Rabczuk, T. Thermal Conductivity of Carbon Nanocoils. *Appl. Phys. Lett.* **2013**, *103*, 233511−233514.

(10) Kim, P.; Shi, L.; Majumdar, A.; McEuen, P. L. Thermal Transport Measurements of Individual Multiwalled Nanotubes. *Phys. Rev. Lett.* **2001**, *87*, 215502−215504.

(11) Pop, E.; Mann, D.; Wang, Q.; Goodson, K. E.; Dai, H. J. Thermal Conductance of An Individual Single-Wall Carbon Nanotube above Room Temperature. *Nano Lett.* **2006**, *6*, 96−100.

(12) Li, Q. W.; Liu, C. H.; Wang, X. S.; Fan, S. S. Measuring The Thermal Conductivity of Individual Carbon Nanotubes by The Raman Shift Method. *Nanotechnology* **2009**, *20*, 1045702.

(13) Yu, C. H.; Saha, S.; Zhou, J. H.; Shi, L.; Cassell, A. M.; Cruden, B. A.; Ngo, Q.; Li, J. Thermal Contact Resistance and Thermal Conductivity of A Carbon Nanofiber. *J. Heat Transfer* **2006**, *128*, 234−239.

(14) Mayhew, E.; Prakash, V. Thermal Conductivity of Individual Carbon Nanofibers. *Carbon* **2013**, *62*, 493−500.

(15) Heremans, J.; Beetz, C. P. Thermal-Conductivity and Thermo-power of Vapor-Grown Graphite Fibers. *Phys. Rev. B: Condens. Matter Mater. Phys.* **1985**, *32*, 1981−1986.

(16) Guo, J. Q.; Wang, X. W.; Wang, T. Thermal Characterization of Microscale Conductive and Nonconductive Wires Using Transient Electrothermal Technique. *J. Appl. Phys.* **2007**, *101*, 063531−063537.

(17) Feng, X.; Wang, X.; Chen, X.; Yue, Y. Thermo-Physical Properties of Thin Films Composed of Anatase TiO_2 Nanofibers. *Acta Mater.* **2011**, *59*, 1934−1944.

(18) Liu, G. Q.; Huang, X. P.; Wang, Y. J.; Zhang, Y. Q.; Wang, X. W. Thermal Transport in Single Silkworm Silks and The Behavior under Stretching. *Soft Matter* **2012**, *8*, 9792−9799.

(19) Hayashida, T.; Pan, L.; Nakayama, Y. Mechanical and Electrical Properties of Carbon Tubule Nanocoils. *Phys. B* **2002**, *323*, 352−353.

(20) Ma, H.; Nakata, K.; Pan, L. J.; Hirahara, K.; Nakayama, Y. Relationship between The Structure of Carbon Nanocoils and Their Electrical Property. *Carbon* **2014**, *73*, 71−77.

(21) Shamsa, M.; Liu, W. L.; Balandin, A. A.; Casiraghi, C.; Milne, W. I.; Ferrari, A. C. Thermal Conductivity of Diamond-Like Carbon Films. *Appl. Phys. Lett.* **2006**, *89*, 1619211−1619213.

(22) Bullen, A. J.; O'Hara, K. E.; Cahill, D. G.; Monteiro, O.; Von Keudell, A. Thermal Conductivity of Amorphous Carbon Thin Films. *J. Appl. Phys.* **2000**, *88*, 6317−6320.

(23) Slack, G. A. Anisotropic Thermal Conductivity of Pyrolytic Graphite. *Phys. Rev.* **1962**, *127*, 694−701.

(24) Smith, A. W.; Rasor, N. S. Observed Dependence of The Low-Temperature Thermal and Electrical Conductivity of Graphite on Temperature, Type, Neutron Irradiation, and Bromination. *Phys. Rev.* **1956**, *104*, 885−891.

(25) Nika, D. L.; Pokatilov, E. P.; Askerov, A. S.; Balandin, A. A. Phonon Thermal Conduction in Graphene: Role of Umklapp and Edge Roughness Scattering. *Phys. Rev. B: Condens. Matter Mater. Phys.* **2009**, *79*, 155413.

(26) Kittel, C. Interpretation of The Thermal Conductivity of Glasses. *Phys. Rev.* **1949**, *75*, 972−974.

(27) Hakovirta, M.; Vuorinen, J. E.; He, X. M.; Nastasi, M.; Schwarz, R. B. Heat Capacity of Hydrogenated Diamond-Like Carbon Films. *Appl. Phys. Lett.* **2000**, *77*, 2340−2342.

(28) Desorbo, W.; Tyler, W. W. The Specific Heat of Graphite from 13-Degrees-K to 300-Degrees-K. *J. Chem. Phys.* **1953**, *21*, 1660−1663.

(29) Xu, Z. L.; Wang, X. W.; Xie, H. Q. Promoted Electron Transport and Sustained Phonon Transport by DNA down to 10 K. *Polymer* **2014**, *55*, 6373−6380.

(30) Liu, J.; Xu, Z. L.; Cheng, Z.; Xu, S.; Wang, X. W. Thermal Conductivity of Ultrahigh Molecular Weight Polyethylene Crystal: Defect Effect Uncovered by 0 K Limit Phonon Diffusion. *ACS Appl. Mater. Interfaces* **2015**, *7*, 27279−27288.

(31) Ho, C.; Powell, R.; Liley, P. Thermal Conductivity of The Elements: A Comprehensive Review. *J. Phys. Chem. Ref. Data* **1974**, *3*, 756−796.

(32) Xie, Y. S.; Xu, Z. L.; Xu, S.; Cheng, Z.; Hashemi, N.; Deng, C.; Wang, X. W. The Defect Level and Ideal Thermal Conductivity of Graphene Uncovered by Residual Thermal Reffusivity at The 0 KLimit. *Nanoscale* **2015**, *7*, 10101−10110.

(33) Ferrari, A. C.; Robertson, J. Interpretation of Raman Spectra of Disordered and Amorphous Carbon. *Phys. Rev. B: Condens. Matter Mater. Phys.* **2000**, *61*, 14095−14107.

(34) Motojima, S.; Chen, Q. Q. Three-dimensional Growth Mechanism of Cosmo-Mimetic Carbon Microcoils Obtained by Chemical Vapor Deposition. *J. Appl. Phys.* **1999**, *85*, 3919−3921.

(35) Li, D. W.; Pan, L. J.; Qian, J. J.; Ma, H. High Efficient Synthesis of Carbon Nanocoils by Catalysts Produced by A Fe and Sn Containing Solution. *Adv. Mater. Res.* **2009**, *60−61*, 251−255.